Stem Cell Research & Therapy

RESEARCH

Open Access

Effects of 3D-printed exosome-functionalized brain acellular matrix hydrogel on neuroinflammation in rats following cerebral hemorrhage

Aobo Zhang[1*], Boyu Sun[1], Chengrui Nan[1], Lulu Cong[1], Zongmao Zhao[1] and Liqiang Liu[1*]

Abstract

Background Exosome-based therapeutics have garnered significant attention for intracerebral hemorrhage (ICH) treatment due to their capacity to regulate metabolic dysregulation, restore cellular homeostasis, and modulate the injury microenvironment via bioactive cargoes such as microRNAs and proteins. However, rapid systemic clearance and enzymatic degradation critically limit their therapeutic efficacy. To address this challenge, we engineered a three-dimensional (3D) bioprinted scaffold capable of encapsulating and sustaining the release of human umbilical cord mesenchymal stem cell-derived exosomes (hUCMSC-exos).

Methods Based on previous research [1–3], the scaffold was composed of a decellularized brain matrix (dECM), gelatin-methacryloyl (GelMA), and silk fibroin (SF) crosslinked with a photoinitiator. hUCMSC-exos were precisely incorporated via extrusion-based 3D bioprinting. Release kinetics were assessed via in vitro elution and in vivo imaging. An ICH rat model received stereotaxic implantation of the exosome-laden scaffold (dECM@exo). Neuroinflammatory markers (IL-6, TNF-α, IL-10) and apoptotic activity (JC-1, Annexin V/PI, TUNEL) were quantified. Neurological outcomes were longitudinally evaluated using the modified Longa scale, Bederson scoring, and sensorimotor tests (rotarod, forelimb placement) at 1, 4, 7 and 14 days post-ICH.

Results dECM@exo demonstrated sustained exosome release over 14 days, significantly promoting neural tissue regeneration while attenuating perihematomal edema. Mechanistically, the scaffold modulated pathological MMP activity and inflammatory cytokine expression, thereby restoring extracellular matrix homeostasis and reducing neuronal apoptosis.

Conclusions The findings demonstrate that the 3D biological scaffold dECM@exo effectively maintains microenvironmental homeostasis in the early stages of ICH and improves outcomes associated with the condition. dECM@exo is poised to serve as a robust platform for drug delivery and biotherapy in ICH treatment, offering a viable alternative for managing this condition.

*Correspondence:
Aobo Zhang
zab199915@163.com
Liqiang Liu
27400950@hebmu.edu.cn

Full list of author information is available at the end of the article

Keywords 3D biological scaffold, dECM, hUCMSC-exos, dECM@exo, Intracerebral hemorrhage, Neuroinflammation

Introduction

Intracerebral hemorrhage (ICH), a devastating neurological emergency characterized by high mortality and disability rates, imposes profound socioeconomic burdens worldwide [1]. Survivors frequently endure persistent motor dysfunction, cognitive deficits, and speech impairments, with up to 50% requiring long-term rehabilitation [2, 3]. While primary mechanical injury caused by hematoma expansion accounts for immediate damage, accumulating evidence underscores that secondary injury cascades—triggered by neuroinflammation, oxidative stress, and blood-brain barrier (BBB) disruption—drive progressive neuronal loss and functional deterioration, even in the absence of hematoma enlargement [4–6]. Despite advances in surgical evacuation and anti-edema therapies, molecular mechanisms governing these secondary pathways remain incompletely elucidated, necessitating innovative strategies to modulate the post-ICH microenvironment [7–9].

Mesenchymal stem cell (MSC) transplantation has emerged as a promising therapeutic avenue for stroke recovery, leveraging their multipotent differentiation, immunomodulatory properties, and paracrine signaling [10–12]. However, clinical translation is hampered by risks of tumorigenicity, immune rejection, and poor engraftment efficiency [13]. Crucially, MSC-derived extracellular vesicles (EVs), particularly exosomes (30–150 nm), have demonstrated comparable therapeutic efficacy to parent cells by mediating intercellular communication via cargo transfer of microRNAs, proteins, and growth factors [14, 15]. Human umbilical cord MSC-derived exosomes (hUCMSC-exos) exhibit neuroprotective, anti-apoptotic, and anti-inflammatory effects in ICH models, attributed to their BBB permeability and capacity to regulate extracellular matrix (ECM) remodeling [16–19]. Recent studies further highlight MSC-exosome-mediated suppression of NLRP3 inflammasome activation and microglial M1 polarization, positioning them as potent modulators of neuroinflammation [20–22].

Despite these advantages, clinical implementation of exosome therapy faces critical challenges. First, the short half-life (<6 h) and rapid clearance of free exosomes necessitate repeated intracranial injections—an impractical approach given the risks of iatrogenic injury [23, 24]. Second, conventional carriers (e.g., liposomes, synthetic polymers) often exhibit cytotoxicity, suboptimal biocompatibility, or mismatched degradation kinetics with neural repair processes [25]. Decellularized extracellular matrix (dECM)-based biomaterials present a compelling solution, as they preserve native tissue-specific biochemical cues (e.g., glycosaminoglycans, fibronectin) while eliminating immunogenic cellular components [26–28]. dECM hydrogels have demonstrated success in osteoarthritis and myocardial repair by promoting site-specific cell homing and ECM deposition [29–31]. Their injectable form and species-independent tolerance further enhance suitability for central nervous system applications [32, 33].

Photocrosslinkable hydrogels, notably gelatin-methacryloyl (GelMA) and silk fibroin (SF) composites, have revolutionized neural tissue engineering by enabling minimally invasive delivery, spatiotemporal control of therapeutic release, and structural mimicry of brain ECM [34–36]. Preclinical studies reveal that such hydrogels attenuate glial scarring, enhance endogenous neurogenesis, and support axonal regrowth in stroke models [37–39]. However, unresolved challenges persist: (1) host immune responses to synthetic crosslinkers (e.g., genipin) may exacerbate neuroinflammation [40]; (2) mismatched mechanical properties between implants and brain parenchyma (~0.1-1 kPa) hinder integration [41]; and (3) most scaffolds fail to replicate the hierarchical architecture of native neural ECM [42].

Decellularization involves the removal of cellular and nuclear components from tissues or organs to prevent initial immune responses while preserving the structure and composition of the natural ECM [40, 41]. The resulting acellular tissue can exist as a porous solid, be ground into powder, or be gelatinized into a hydrogel. Well-preserved acellular ECMs contain comparable concentrations and proportions of glycosaminoglycans (GAGs), fibronectin, and adhesion proteins, which can stimulate regenerative responses specific to the tissue or organ [42]. Additionally, given the conserved nature of these molecules across species, heterologous receptors exhibit good tolerance to dECM [43]. The injectable form of dECM is particularly well-suited for central nervous system applications, such as nerve regeneration [44–45].

To address these limitations, on the basis of the original research [1, 2], we engineered a 3D bioprinted scaffold synergizing dECM's bioactivity with photocurable GelMA/SF's tunable mechanics. This platform, termed dECM@exo, encapsulates hUCMSC-exos via extrusion-based bioprinting to achieve sustained exosome release while mimicking the brain's native viscoelasticity (~2 kPa). Using a collagenase IV-induced striatal ICH model, we evaluated dECM@exo's capacity to mitigate neuroinflammation, suppress MMP-9-mediated ECM degradation, and restore neurological function. Our findings establish dECM@exo as a multifunctional theranostic platform that synchronizes exosome delivery with

microenvironmental reprogramming, offering a transformative strategy for ICH management (Scheme 1).

Materials and methods

All experimental protocols were approved by the Institutional Animal Care and Use Committee (Approval No. 2024-R190) and conducted in accordance with NIH guidelines.

Materials

Deoxyribonuclease I (DNase I, bovine pancreas; DN25, CAS 9003-98-9) and Ribonuclease A (V900498, CAS 9001-99-4) were procured from Sigma-Aldrich. Gelatin methacrylate (GelMA, A2033, CAS 9005-38-3; medium viscosity), pepsin (P0103, CAS 9001-75-6), and analytical-grade reagents were obtained from TCI Development. Gelatin (AC08BA0009, CAS 9000-70-8; Bloom index: 240–270) was purchased from Sangon Biotech.

Decellularized brain matrix (dECM) Preparation

Male Sprague-Dawley rats aged 10 to 12 weeks were maintained in a controlled environment at 25 °C with a 12-hour light-dark cycle. The rats weighed between 250 and 300 g and had free access to food and water. Brain tissues were harvested through a detailed decellularization process involving low-osmotic treatment with 0.1 mM phenylmethylsulfonyl fluoride (PMSF) for 24 h, followed by sequential treatment with 0.1% sodium dodecyl sulfate (SDS) for 24 h, 1% Triton X-100 for 48 h, and enzymatic treatments with a nuclease mixture (DNase and RNase for 12 h) and 5% peracetic acid for 2 h. The processed tissue was lyophilized and sterilized using gamma irradiation before storage.

Characterization of dECM

Both native and decellularized rat brain tissues were characterized using electron microscopy and histological techniques. Scanning electron microscopy (SEM) (GeminiSEM 300, Zeiss) was employed after gold plating to assess the cross-sectional morphology of native and dECM samples. DNA quantification was performed utilizing a Genomic DNA Kit (TIANGEN, Beijing, China), with concentrations measured at 260 nm using a microplate spectrophotometer (Thermo Fisher Scientific, USA). Hematoxylin and eosin (HE) staining and Masson staining were used to evaluate cell distribution, while

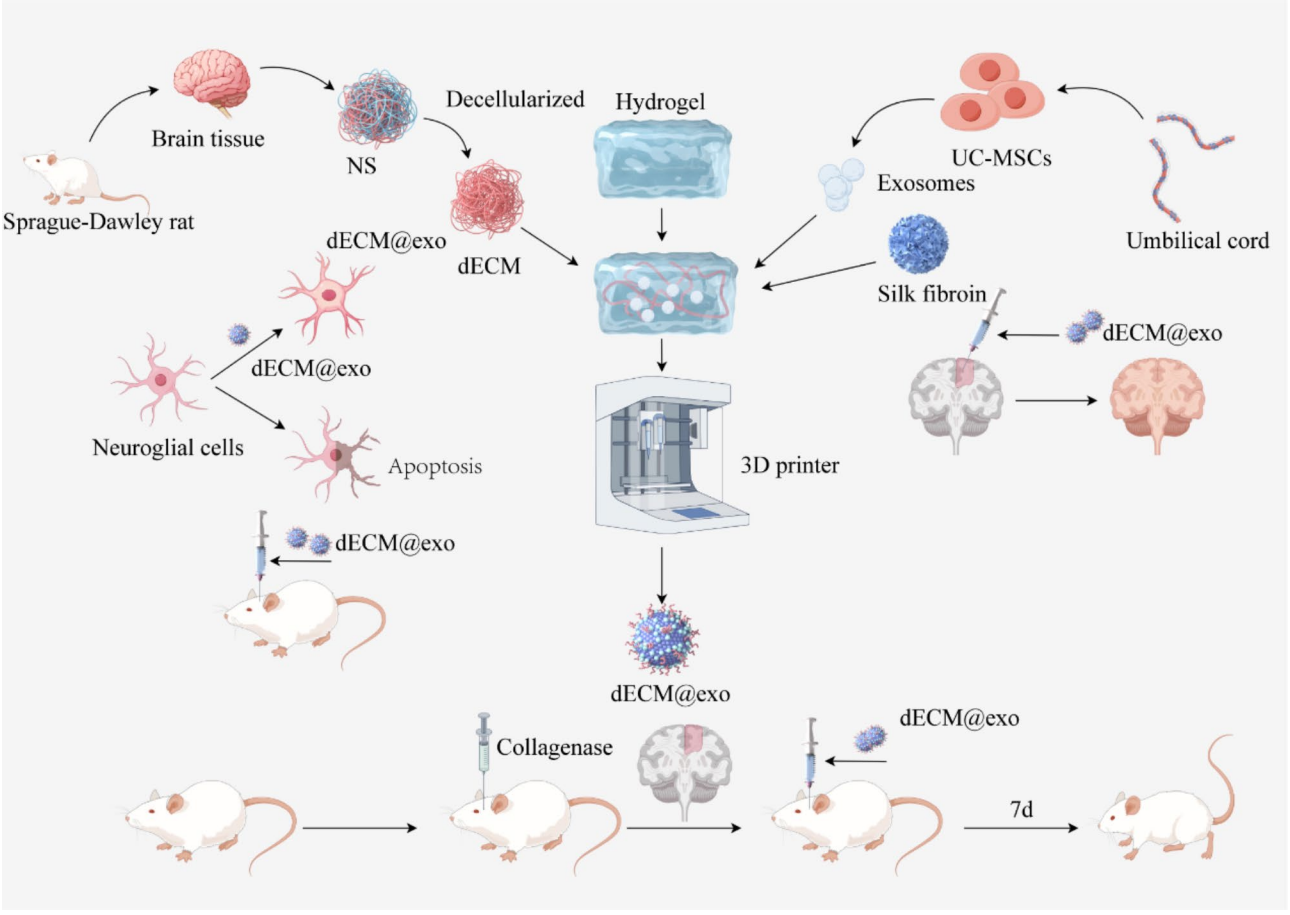

Scheme 1 dECM@exo synthesis and its mechanism for treating ICH

Sirius red staining quantified proteoglycan and collagen distribution. Total collagen content was assessed using a collagen detection kit (ab222942, Abcam).

Preparation of Bioink

Freeze-dried dECM was milled in liquid nitrogen. A total of 100 mg of dECM powder was digested in 3 mL of 0.01 M hydrochloric acid (pH 2.0) with 45 mg of pepsin for 24 h. Circular dichroism (CD) spectroscopy was used to evaluate the effects of hydrochloric acid on dECM, scanning from 190 to 260 nm. The pH of the dECM solution was then adjusted from 3.3 to 3.6 to 7.0–7.2 using 10 M NaOH. A 15% (w/v) gelatin and 3% (w/v) silk fibroin mixture was dissolved in 3 mL of distilled water at 55 °C for 30 min, then combined with the pH-adjusted dECM solution, pasteurized, resulting in a 3D biological ink.

Rheological characterization of Bioink

The rheological properties of the bioink were assessed using a rotational rheometer (Malvern Kinexus Ultra+) with 25 mm diameter plates. Viscosity comparisons between bioink and dECM hydrogel were performed over a temperature range of 0°C to 50°C using strain sweep analysis. The amplitude sweep analyzed strain-dependent storage modulus (G') and loss modulus (G") over a strain range of 0.01–100 at a frequency of 10% rad s – 1, with all measurements repeated in triplicate.

Microarchitecture of Bioink

The surface ultrastructure of the bioink was analyzed via SEM. The bioink was freeze-dried, fixed in 2.5% glutaraldehyde overnight at 4 °C, washed with PBS, dehydrated with graded ethanol, and gold sputter coated for observation on a JSM-5600LV SEM.

Biocompatibility of Bioink

Subcutaneous injections of 400 μL of bioink were administered to the backs of 10-week-old Sprague-Dawley rats. Grafts were harvested at 1, 2, 4, and 8 weeks post-injection and subsequently embedded in paraffin for HE staining.

Printing and in vitro culture of 3D biological scaffold (dECM@exo)

A bioprinting system (Bio-Architect®-WS; Hangzhou Regenovo Biotechnology, Ltd.) was employed to print dECM@exo. The printer nozzle diameter was set to 340 μm. The nozzle and chamber temperatures were maintained at 20 °C and 4 °C, respectively, while pneumatic pressure was adjusted to optimize the nozzle scanning speed, ranging from 0.2 to 0.4 kPa with a scanning speed of 6 mm/s to ensure the resulting dECM@exo took on a cubical shape. The hUCMSC-exos were thoroughly mixed with bio-ink (1×10^6 cells /mL) and cultured for 7 days for printing. Immediately post-printing, the formed 3D cell-laden scaffolds ($2 \times 2 \times 1$ mm^3) were soaked in a 5% calcium chloride solution to cross-link for 5 min. The cell-loaded 3D scaffolds were then incubated for 1, 4, 7 and 14 days, followed by a live/dead assay kit (Molecular Probes, Inc., Cat. No. L3224) according to the manufacturer's protocol to evaluate cell viability within the 3D cell-laden scaffolds.

Characterization of 3D biological scaffold (dECM@exo)

The 3D biological scaffold (dECM@exo) was characterized using Fourier-transform infrared (FT-IR) spectroscopy (Nicolet iS10), with 32 scans covering the range of 4000 to 400 cm^{-1}. SEM (GeminiSEM 300, Zeiss) was also utilized to visualize the scaffold's porous structure. The influence of scaffold's injectability were assessed by monitoring changes in viscosity at varying shear rates.

Isolation and characterization of hUCMSC-exos

Umbilical cord tissue was supplied by Hebei Benyuan Biotechnology Co. Ltd. Mesenchymal stem cells were cultured in a medium containing 5% CO2, 10% FBS (excluding hUCMSC-exos), and 1% mycillin for 48 h to collect cell supernatants. Flow cytometry was used to identify surface markers CD73, CD90, and CD105. hUCMSC-exos were isolated through cryogenic ultracentrifugation. Cells in the supernatant were centrifuged at 300 g for 10 min to remove debris, followed by further centrifugation at 2000 g and 10,000 g to eliminate smaller debris and apoptotic bodies, respectively. Ultracentrifugation at 100,000 g for 70 min at 4 °C was performed to isolate hUCMSC-exos, which were then suspended in PBS and stored at -80 °C. The protein concentration of hUCMSC-exos was determined using a BCA assay, and Western blotting (Abclonal, China) was conducted to identify CD63 and CD9 as hUCMSC-exos markers. Transmission electron microscopy (TEM) and nanoparticle tracking analysis (NTA) were utilized to assess the morphology and size distribution of hUCMSC-exos. TEM displayed a cup-shaped morphology for hUCMSC-exos, while NTA revealed a particle size distribution between 30 and 150 nm, with a peak near 110 nm. The total protein content of hUCMSC-exos, standardized by BCA, was found to be 0.5 mg/mL.

In vitro release test and pharmacokinetic test

The release profile of hUCMSC-exos from dECM@exo was quantified using a rat CD63 ELISA kit (Shanghai Meimian, China). A total of 100 μL of prepared dECM@exo containing 1 μg of hUCMSC-exos was placed in the upper compartment of a Transwell insert within a 24-well plate (Corning, China). Subsequently, 200 μL of PBS was added to the lower compartment. On days 0, 4, 8, 12, 16,

20, 24, and 28, 100 μL of PBS (pH = 5.5) was collected and replenished with 100 μL of fresh PBS to determine the number of hUCMSC-exos released.

In vivo degradation of dECM@exo

Luciferase-labeled dECM@exo was orthotopically implanted into Sprague-Dawley (SD) rats, and its spatiotemporal release and degradation kinetics were non-invasively monitored using an in vivo imaging system (IVIS Lumina XRMS, PerkinElmer) on days 1, 4, 7, and 14 post-implantation. Bioluminescence signals were quantified to assess scaffold integrity and exosome retention.

Isolation of primary astrocytes

Neonatal Sprague-Dawley rats were anesthetized with 3% isoflurane (RWD Life Science, Shenzhen, China), and brains were aseptically excised into ice-cold Dulbecco's Hank's Balanced Salt Solution (D-HBSS; Gibco, 14175095). Under a stereomicroscope (Leica M80), the cerebellum, brainstem, and hippocampus were dissected, followed by meticulous removal of the pia mater and vasculature. Cortical tissue was minced into 1 mm^3 fragments and digested in 0.25% trypsin-EDTA (Gibco, 25200072) containing 50 U/mL DNase I (Sigma, DN25) at 37 °C for 5 min with gentle agitation. The homogenate was filtered through a 70 μm cell strainer (Falcon, 352350), centrifuged at 1,000 ×g for 2 min (Eppendorf 5430R), and resuspended in DMEM/F12 medium (Gibco, 11330032) supplemented with 10% FBS (Gibco, 10099141). Cells were seeded into T75 flasks and maintained at 37 °C/5% CO_2, with medium replaced after 24 h to eliminate debris.

Exosome tracking in astrocytes

Primary astrocytes were treated with 10 μg/mL PKH26-labeled dECM@exo (Sigma, MINI26) for 12 h. Cells were fixed with 4% paraformaldehyde (PFA; Sigma, P6148), permeabilized with 0.1% Triton X-100 (Sigma, T8787), and stained with Alexa Fluor 488-phalloidin (1:500; Invitrogen, A12379) for 60 min at RT. Nuclei were counterstained with DAPI (1 μg/mL; Sigma, D9542). Fluorescence images were acquired using a confocal microscope.

Cytotoxicity assay

Cell viability was assessed using the CCK-8 assay (ZOMANBIO, ZP328). Astrocytes (5×10^3 cells/well) in 96-well plates were treated with dECM@exo or controls for 24 h. After replacing medium with 10% CCK-8 reagent, absorbance at 450 nm was measured using a microplate reader (BioTek Synergy H1). Survival rates were normalized to untreated controls.

Flow cytometric analysis of apoptosis

Cells were harvested, washed in PBS, and stained with Annexin V-FITC (0.5 μg/mL; BD Biosciences, 556547) and propidium iodide (PI; 50 μg/mL; Sigma, P4170) for 15 min at RT in the dark. Apoptosis was quantified via BD FACSAria III, with data analyzed using FlowJo v10.8.1 (BD Biosciences). Early (Annexin V^+/PI^-) and late (Annexin V^+/PI^+) apoptotic populations were combined for total apoptosis rates.

Mitochondrial membrane potential assessment

Astrocytes seeded in confocal dishes were incubated with 5 μM JC-1 dye (Beyotime, C2006) for 30 min at 37 °C. Fluorescence was imaged at 488 nm (green, monomeric) and 594 nm (red, J-aggregates) using a Leica SP8 confocal microscope.

Immunofluorescence staining

Cells from SHAM, ICH, dECM, and dECM@exo groups were fixed in 4% PFA, blocked with 5% BSA (Sigma, A7906), and incubated overnight at 4 °C with primary antibodies: GFAP (1:200; Abcam, ab7260), TLR4 (1:200; Abcam, ab13556), and NF-κB/P65 (1:200; Abcam, ab307840). Alexa Fluor 488- or 594-conjugated secondary antibodies (1:500; Abcam, ab150116) were applied for 2 h at RT. Nuclei were stained with DAPI.

Western blotting

Nuclear and cytoplasmic fractions were isolated using the Minute™ Extraction Kit (Invent, SC-003). Proteins (30 μg/lane) were separated on 10% SDS-PAGE gels and transferred to PVDF membranes (Millipore, IPFL00010). After blocking with 5% non-fat milk, membranes were probed overnight at 4 °C with primary antibodies, followed by HRP-conjugated secondaries (1:5,000; Abcam, ab6721). Bands were visualized via chemiluminescence (Li-COR Odyssey) and quantified using ImageJ v1.53.

Animal surgery and ICH model

Male SD rats (200–250 g; Vital River, Beijing) were housed under 23 ± 1 °C, 55 ± 2% humidity, with ad libitum access to food/water. ICH was induced by stereotaxic injection of 1 μL collagenase IV (0.5 U/μL; Sigma, C5138) into the right striatum (coordinates: 0.24 mm posterior to bregma, 3 mm depth) at 0.2 μL/min. Sham controls received saline. At 6 h post-ICH, rats received intracerebral injections of 200 μL saline (SHAM/ICH) or 100 μg dECM/dECM@exo.

Nissl staining and brain water content

Coronal brain Sect. (20 μm) were deparaffinized, stained with 0.1% toluidine blue (Leagen Biotech, LB-TB01) at 55 °C for 30 min, and imaged (Leica DM2500). Brain

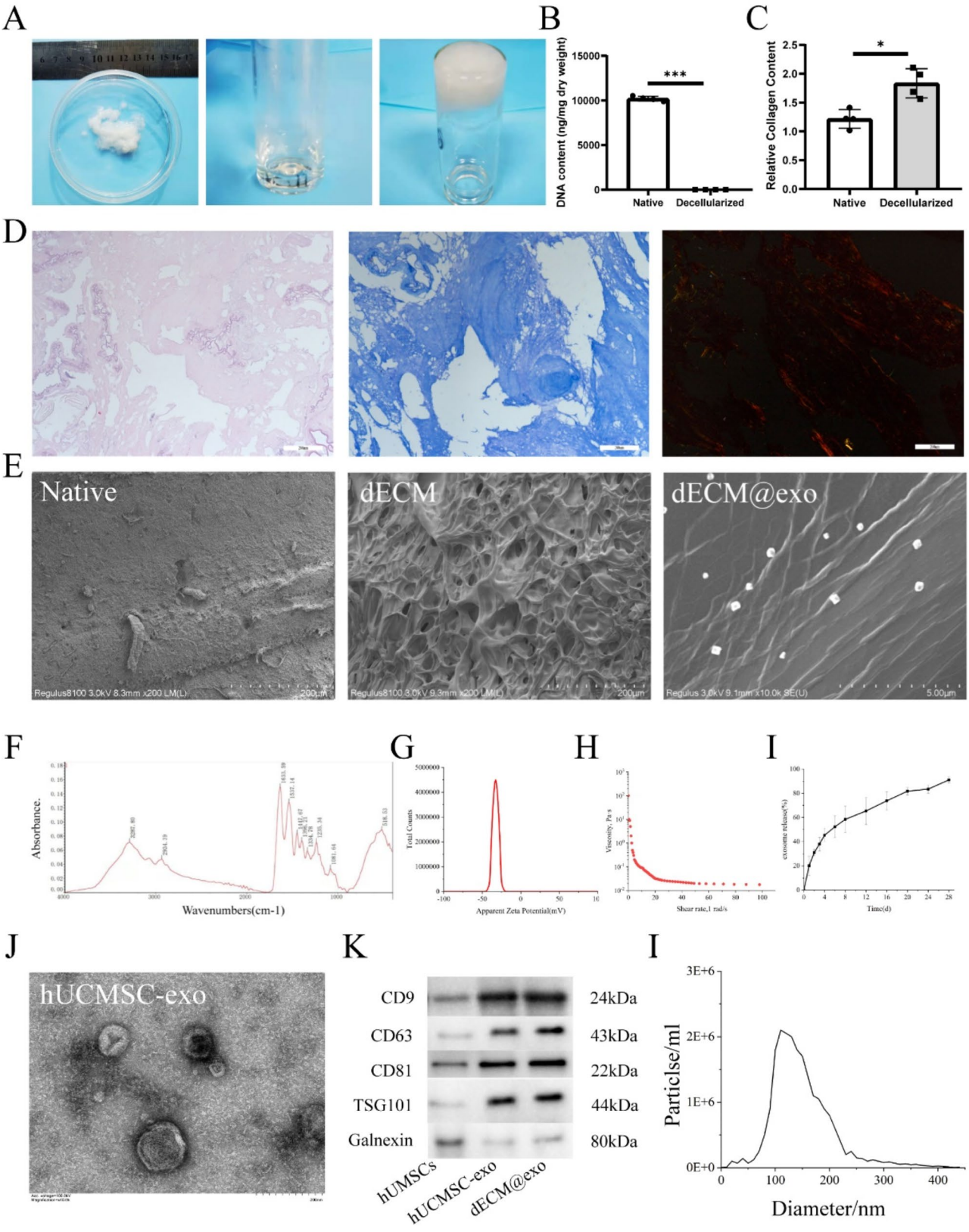

Fig. 1 (See legend on next page.)

(See figure on previous page.)

Fig. 1 Preparation and characterization of dECM@exo. (**A**) Image of brain decellularization and hydrogel preparation. (**B**) Quantitative determination of DNA content ($n = 3$). (**C**) Quantitative determination of collagen retention ($n = 3$). (**D**) HE and Masson staining demonstrate decellularization, and Sirius red staining confirms the retention of collagen fibers. (**E**) SEM analysis of ECM, dECM and dECM@exo. (**F**) FTIR of NS and dECM spectra, the peak at 1290 cm^{-1} corresponds to the NH2 group. C = O stretching was detected at a wavelength of 1625 cm^{-1}. (**G**) Zeta potential of exosomes. (**H**) Viscosity change of dECM@exo hydrogel at shear rates from 1 rad/s to 100 rad /s. (**I**) Controlled release curve of dECM@exo ($n = 3$). (**J**) TEM analysis of hUCMSC-exos. (**K**) Western blot identification results. (**L**) Dynamic light scattering analysis of hUCMSC-exos. Scale bars: D, 200 μm; E, 200 μm/5μm; J, 200 nm. Data were expressed as mean ± standard deviation. *$p < 0.05$, **$p < 0.01$, ***$p < 0.001$, ****$p < 0.0001$

water content was calculated as [(wet weight – dry weight)/wet weight] × 100% after 24 h drying at 100 °C.

Neurobehavioral assessment

Neurological deficits were evaluated at 1, 4, 7 and 14 days post-ICH using: Forelimb placement test: Success rate (%) of ipsilateral limb placement over 10 trials. Corner turn test: Percentage of right turns in a 30° corner. Bederson score: 0 (normal) to 3 (severe circling). Longa score: 0 (no deficit) to 4 (coma).

Enzyme-linked immunosorbent assay (ELISA)

Cell supernatants or animal serum samples were collected and centrifuged to remove sediment. ELISA kits (Abclone, RK00020, China) were employed to measure levels of TNF-α, IL-1β, IL-10, MMP-2, MMP-9, TIMP-1 and TIMP-2 in the samples.

RT-qPCR

RNA extraction was conducted using an RNA extraction kit, followed by quantification of RNA concentration with a UV spectrophotometer at 260 nm. The extracted RNA was reverse transcribed into cDNA using a PCR kit. RT-qPCR analysis was performed following the manufacturer's instructions with the SYBR Premix Ex Tap™ II Kit (Takara). GAPDH served as the internal control, and relative gene expression was determined using the 2-ΔΔCt method.

Statistical analysis

Data are expressed as mean ± SD ($n \geq 3$). Normality was assessed via Shapiro-Wilk test. Parametric data were analyzed by one-way ANOVA with Tukey's post-hoc test; non-parametric data used Kruskal-Wallis test (GraphPad Prism 8.0). Significance: *$p < 0.05$, **$p < 0.01$, ***$p < 0.001$.

Results

Preparation and characterization of dECM@exo

A three-dimensional (3D) biocompatible scaffold derived from a brain acellular matrix was fabricated (Fig. 1A). DNA analysis indicated that over 99% of the DNA content was successfully removed from the dECM (Fig. 1B). Furthermore, the collagen content in dECM exceeded that of fresh brain tissue (Fig. 1C). Hematoxylin and eosin (HE) and Masson staining confirmed these alterations, while Sirius red staining illustrated the collagen structure (Fig. 1D). Following freeze-drying, dECM@exo displayed a porous three-dimensional architecture (Fig. 1E).

Fourier-transform infrared (FTIR) analysis identified various peaks, including C–N at 1047 cm^{-1} and NH2 at 1290 cm^{-1}, confirming the presence of numerous positively charged groups within the dECM (Fig. 1F). Zeta potential measurements revealed that hUCMSC-exos exhibited a value of – 32.7 mV, indicating a strong binding affinity of hUCMSC-exos to the dECM (Fig. 1G).

The rheological properties of dECM@exo were evaluated to assess its mechanical behavior. A progressive increase in shear rate correlated with a decrease in viscosity, suggesting favorable injectability (Fig. 1H). Sustained release analysis demonstrated that dECM@exo exhibited excellent sustained release properties, with a gradual release of hUCMSC-exos over 28 days (Fig. 1I).

hUCMSC-exos characterization confirmed their biological activity. Transmission electron microscopy (TEM) revealed the characteristic cup-shaped morphology of hUCMSC-exos (Fig. 1J). Western blot analysis validated the presence of exosomal markers CD9, CD63, CD81 and TSG101 in the samples (Fig. 1K). Dynamic light scattering indicated a size distribution of hUCMSC-exos ranging from 30 to 150 nm, with a peak size of approximately 110 nm (Fig. 1L). These results confirm that hUCMSC-exos possess exosomal characteristics and are suitable for further study.

The dECM@exo exhibited excellent injectability (Fig. 2A), with scaffolds measuring 2 mm × 2 mm × 1 mm successfully produced via 3D printing (Fig. 2B). For drug delivery, dECM@exo containing hUCMSC-exos was synthesized at varying concentrations (50, 100, 200, 300, 400, and 500 μg/mL). To solubilize hUCMSC-exos, 3 mL of acetic acid was mixed with the scaffold for three hours. Following centrifugation at 3500 RPM for 15 min, the absorbance of the supernatant was measured using ELISA, indicating that hUCMSC-exos encapsulation efficiency improved with increasing concentration (Fig. 2D).

In vivo evaluation of dECM@exo

Shear forces applied during the 3D printing process may potentially compromise the integrity of hUCMSC-exos within the printed constructs. Additionally, cytotoxic residues derived from dECM@exo could adversely affect cellular viability. To address these concerns, we performed live/dead assays to assess the survival of hUCMSCs encapsulated within dECM@exo. On day 1, hUCMSCs

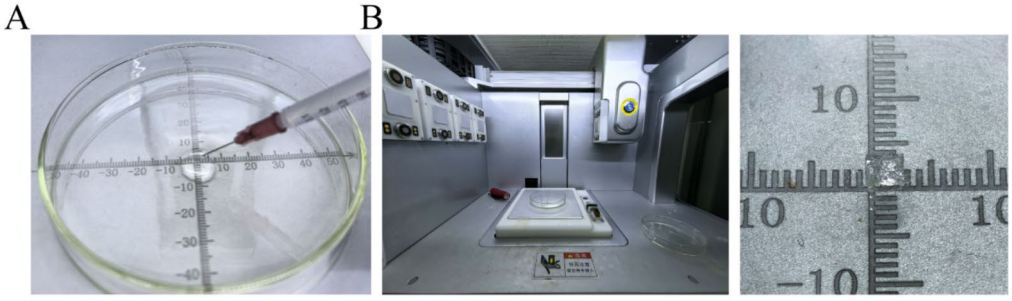

D

hUCMSC-ex Concentration (ug/ml)	Encapsulation Efficiency %	
	dECM	dECM@exo
50	32.13	34.52
100	72.15	74.66
200	82.81	87.58
300	83.66	94.98
400	87.24	98.15
500	89.81	99.10

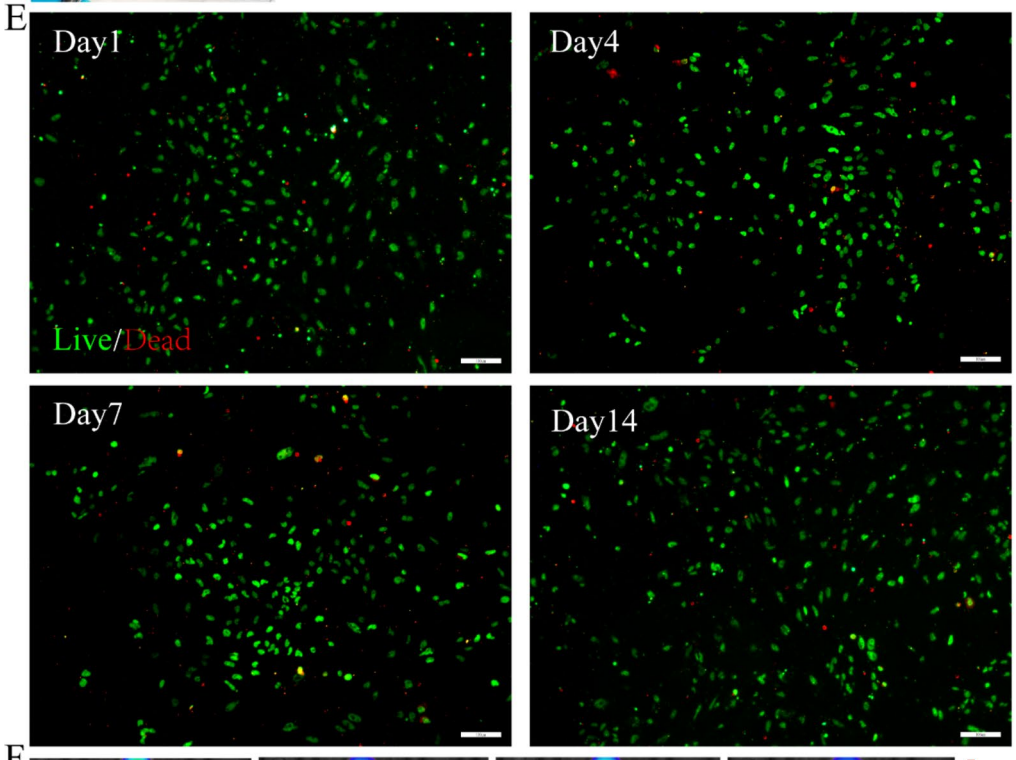

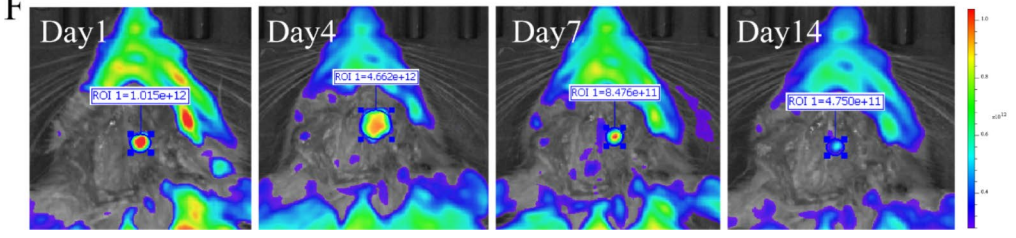

Fig. 2 (See legend on next page.)

(See figure on previous page.)

Fig. 2 Evaluation of dECM@exo. (**A**) dECM@exo exhibited excellent injectable. (**B**) 3D printed 2 mm x 2 mm x 1 mm dECM@exo. (**C**) dECM@exo orthotopic transplantation. (**D**) Examination of the relationship between microsphere particle size and polydispersity index (PDI) at different hUCMSC-exos concentrations ($n = 3$). (**E**) Exhibiting green fluorescence (live cells with calcein AM) and red fluorescence (dead cells with EthD-1) as observed under a laser confocal microscope. (**F**) In vivo biodistribution and degradation of luciferase-labeled dECM@exo. Scale bars: E, 100 μm. Data were expressed as mean ± standard deviation. *$p < 0.05$, **$p < 0.01$, ***$p < 0.001$, ****$p < 0.0001$

exhibited high viability within the scaffold. Notably, cell survival remained elevate after 14 days of culture (Fig. 2E). Consistent with prior studies [1], dECM@exo retained its original 3D microstructure prior to degradation, providing a substrate for cell encapsulation and establishing an optimal microenvironment for cellular survival. Cells transplanted into dECM@exo secreted matrix proteins, locally reconstructing their own extracellular matrix (ECM), thereby enabling refined tissue remodeling even after scaffold degradation. To evaluate in vivo absorption and degradation kinetics, luciferase-labeled dECM@exo was implanted into Sprague-Dawley rats. Longitudinal bioluminescence imaging revealed gradual scaffold degradation and exosome release over time (Fig. 2F).

Immunofluorescence analysis of cultured cells displayed that all cels expressed glial fibrillary acidic protein (GFAP), a specific marker for astrocytes (Fig. 3A). To track hUCMSC-exos in vitro, PKH26-labeled dECM@exo was applied to primary rat astrocytes, which were stained with phalloidin. Red-labeled hUCMSC-exos nanoparticles were found distributed in the cytoplasm and processes of astrocytes (Fig. 3B). The number of astrocytes increased over time, while the proportion of proliferating cells decreased (Fig. 3C). The percentage of Ki67-positive astrocytes in the dECM@exo group was significantly higher than in the NC group (Fig. 3D). Cell viability, assessed via the CCK-8 method, indicated a slight increase in cell viability in both the dECM and dECM@exo groups compared to the NC group, although the differences were not statistically significant (Fig. 3E). Nearly all cells cultured on dECM and dECM@exo remained viable on days 1, 3, and 7. The number of viable cells progressively increased with culture duration, with the most significant growth observed in the dECM@exo group.

dECM@exo mitigates ICH-induced inflammatory response

dECM@exo exhibited anti-inflammatory effects in an ICH model using primary astrocytes stimulated with Hemin (Fig. 3F). ELISA results indicated that ICH stimulation led to a significant increase in IL-1β (Fig. 3G) and TNF-α (Fig. 3H) levels in astrocyte supernatants, both of which were effectively reduced by dECM@exo treatment. In contrast, IL-10 levels demonstrated an inverse pattern (Fig. 3I). Western blot analysis revealed a prominent increase in TLR4, NF-κB/P65, and phosphorylated P65 (p-P65) levels in astrocytes subjected to Hemin, compared to the control group. Treatment with dECM@exo significantly downregulated the expression of these proteins (Fig. 3J). Quantitative data indicated a substantial decrease in TLR4 protein levels following dECM@exo intervention (Fig. 3K). RT-PCR analysis demonstrated an increase in TLR4 mRNA levels following ICH stimulation compared to the control group. However, the administration of dECM@exo had no effect on TLR4 mRNA expression (Fig. 3L).

dECM@exo inhibits astrocyte apoptosis

To assess the impact of dECM@exo on cell apoptosis, we utilized JC-1 staining (Fig. 4A and B) along with flow cytometric apoptosis analysis (Fig. 4C and D). Our results indicated that the reduction of apoptosis in the dECM@exo group was notably more significant compared to both the ICH group and the dECM group. This corroborated the finding that dECM@exo is effective in decreasing astrocyte apoptosis.

Levels of matrix metalloproteinases (MMP-2 and MMP-9) and their inhibitors (tissue inhibitor of metalloproteinases, TIMP-1 and TIMP-2) were quantified via ELISA. Intracerebral hemorrhage (ICH) triggered a significant elevation in MMP-2 and MMP-9 levels compared to sham controls (Figs. 4E-F), indicative of exacerbated extracellular matrix (ECM) degradation, blood-brain barrier (BBB) disruption, and cerebral edema. Compensatory upregulation of TIMP-1 and TIMP-2 was observed (Figs. 4G-H); however, the MMP-9/TIMP-1 ratio remained > 1, suggesting persistent ECM catabolism. Remarkably, dECM@exo intervention normalized this imbalance, reducing MMP-2/9 levels by 48% and 52%, respectively, while elevating TIMP-1/2 by 1.7- and 1.5-fold.

dECM@exo alleviates brain damage in ICH rats

HE staining revealed reduced pathological damage in the dECM@exo group, with notable cell necrosis observed in both the ICH and dECM groups (Fig. 5A). The permeability of the blood–brain barrier was evaluated using the Evans blue leakage technique, revealing an observably increase in extravasation in the ICH group compared to the sham group. Additionally, the administration of dECM@exo improved the worsening of extravasation, as depicted in Fig. 5B. TEM analysis showed that the dECM@exo treatment significantly mitigated mitochondrial cristae loss, outer membrane rupture, vasodilation, and inflammatory extravasation in ICH-injured

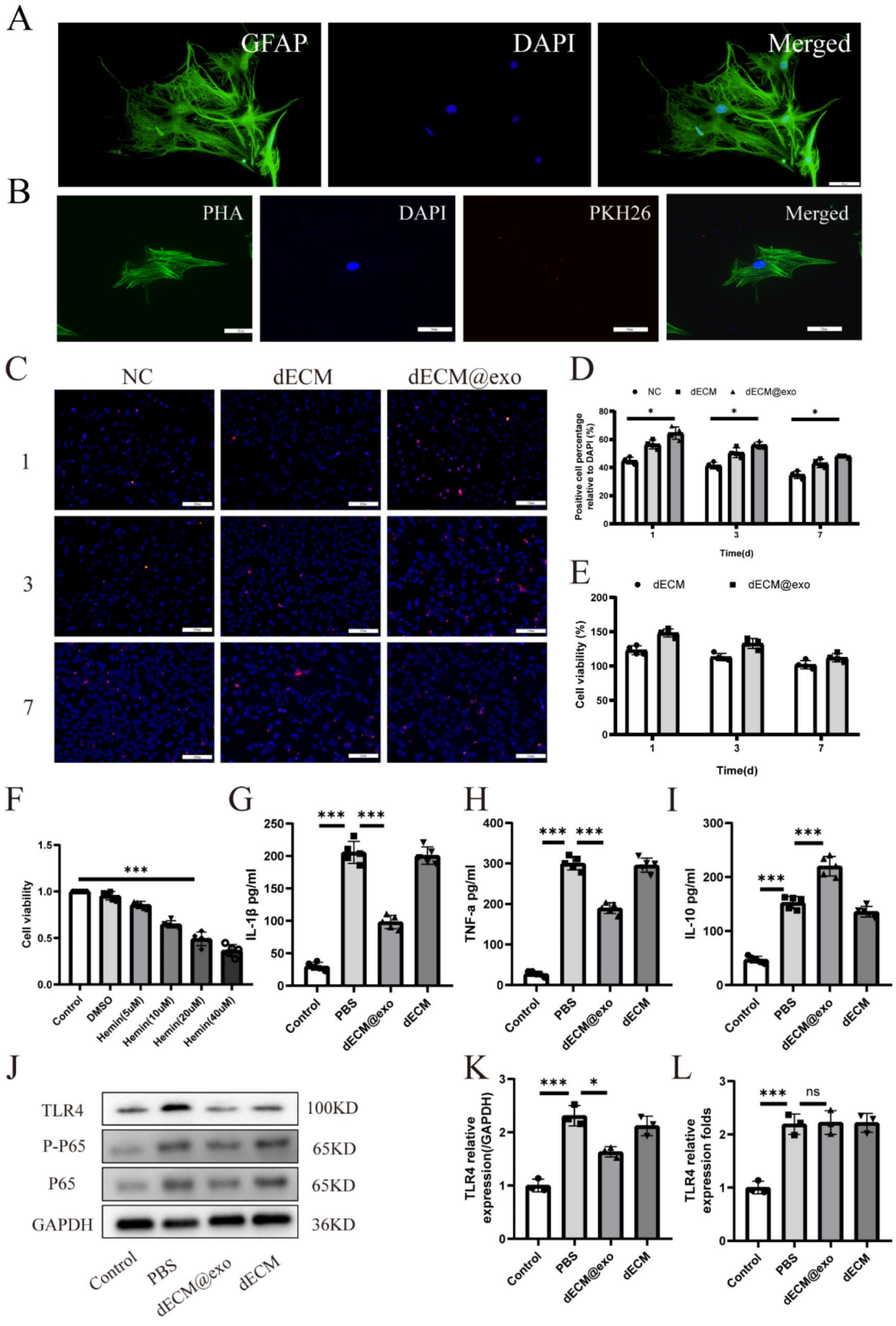

Fig. 3 (See legend on next page.)

(See figure on previous page.)

Fig. 3 dECM@exo inhibits ICH-induced inflammation and improves MMP in astrocytes. (**A**) Morphological characteristics of primary astrocytes and their specific marker GFAP. (**B**) dECM@exo transfected into astrocytes. (C, D) Quantitative detection of the proportion of cells expressing Ki67($n=3$). (**E**) Cell viability of cells cultured with dECM or dECM@exo. (**F**) Cell viability of cells cultured with Hemin. (**G**-**I**) ELISA analysis of IL-1β, TNF-α, and IL-10 levels in astrocyte supernatants. (**J**) Western blot of TLR4 and NF-κB/P65, p-P65. (**K**) Statistical analysis of TLR4. (**L**) Statistical analysis of TLR4 mRNA. Scale bars: A and B, 50 μm; C, 100 μm. Data were expressed as mean ± standard deviation. *$p<0.05$, **$p<0.01$, ***$p<0.001$, ****$p<0.0001$

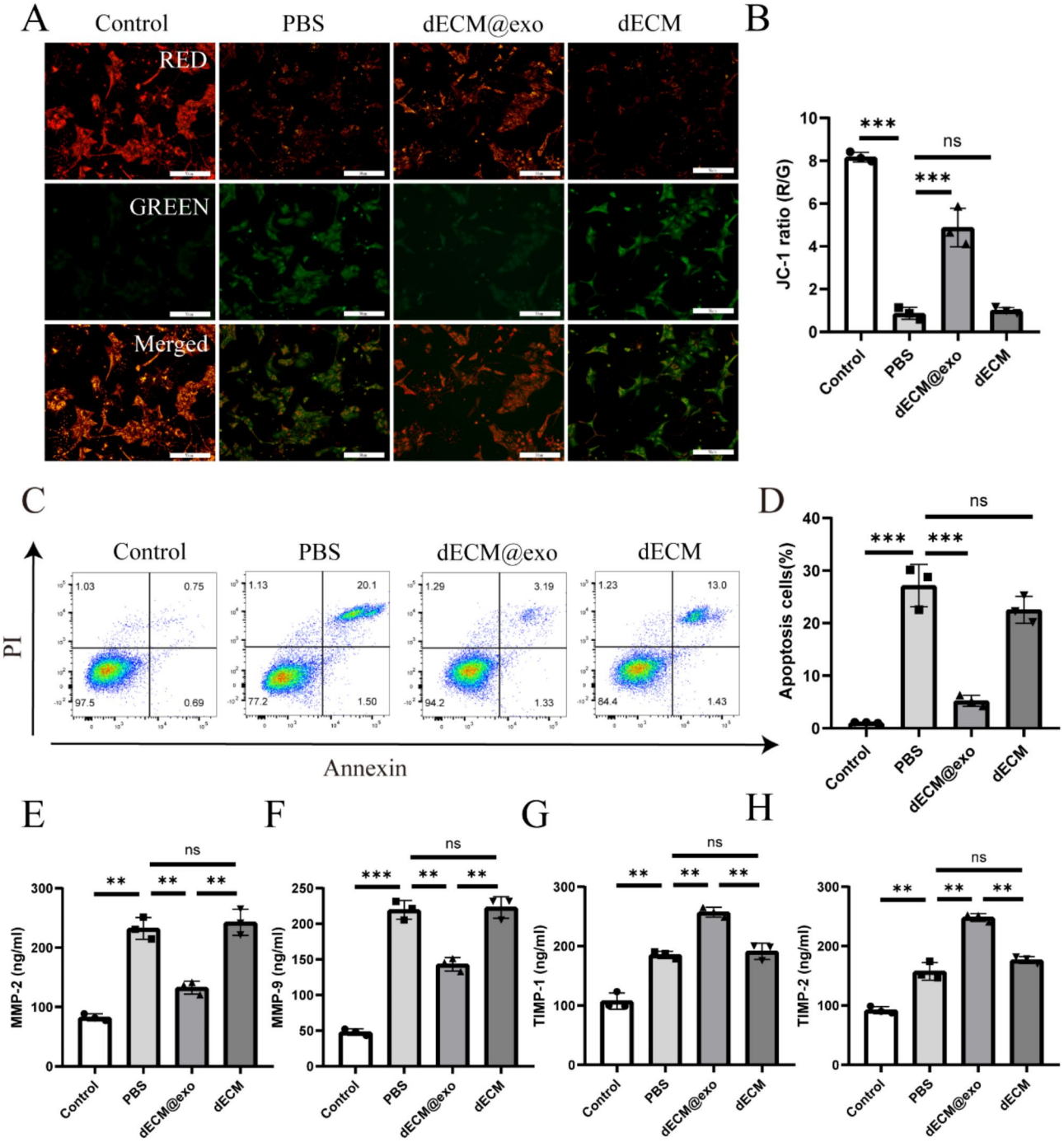

Fig. 4 dECM@exo inhibits astrocyte apoptosis. (**A**) Representative images of JC-1 staining. (**B**) Statistical plot of astrocyte JC-1 fluorescence (red/green) ratio ($n=3$). (**C**) Representative images of apoptosis by flow cytometry. (**D**) Statistical diagram of astrocyte apoptosis ($n=3$). (**E**-**H**) ELISA analysis of MMP-2, MMP-9, TIMP-1 and TIMP-2 levels in astrocyte supernatants. Scale bars: A 50 μm. Data were expressed as mean ± standard deviation. *$p<0.05$, **$p<0.01$, ***$p<0.001$, ****$p<0.0001$

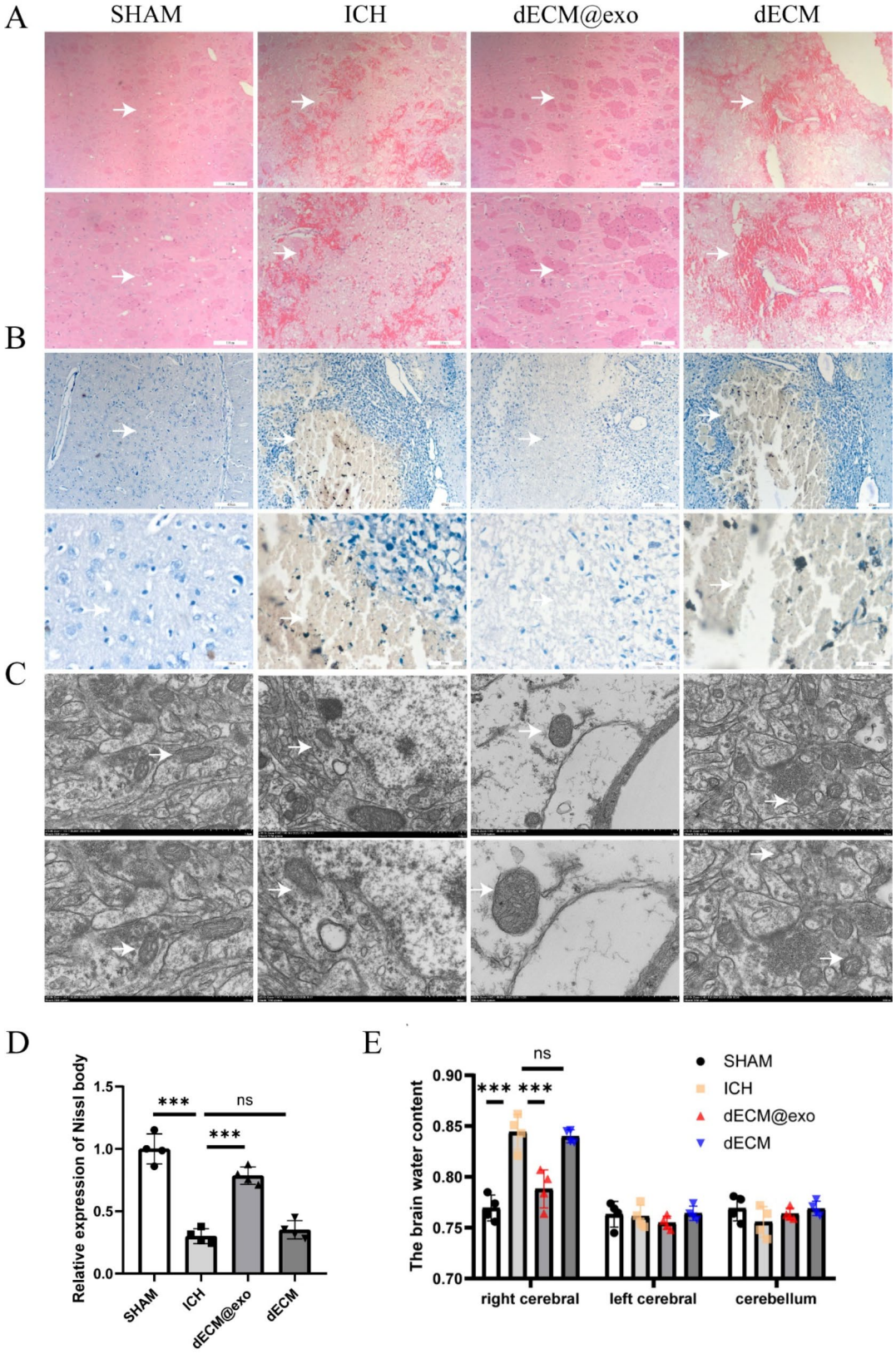

Fig. 5 dECM@exo alleviates brain damage caused by ICH. (**A**) HE staining of rats in different groups. (**B**) Representative pictures of the Evens blue extravasation of different groups. (**C**) Representative TEM images of inflammatory exudation in rats from different groups. (**D**) Nissl staining in the Rat of different groups ($n=4$). (**E**) Detect the brain water content of each group and evaluate the effect of treatment on cerebral edema ($n=4$). Scale bars: B 400 μm/100μm; C, 4 μm/1μm. Data were expressed as mean ± standard deviation. *$p<0.05$, **$p<0.01$, ***$p<0.001$, ****$p<0.0001$

brain tissue, compared to the control and dECM groups (Fig. 5C). Nissl corpuscle changes and cerebral edema were assessed on day five post-ICH to evaluate treatment efficacy. Increased Nissl bodies were observed in the dECM@exo treatment group compared to the ICH group, accompanied by a significant reduction in brain water content (Fig. 5D and E).

To evaluate the effects of dECM@exo on neurological impairment following ICH, we performed neurobehavioral assessments in rats at 1, 4, 7 and 14 days post-injury. Sensorimotor function was quantitatively assessed using the forelimb placement and corner turning tests, while overall neurological function was evaluated using the Longa and Bederson scoring systems. Results showed that dECM@exo treatment significantly improved performance in both the corner turning test (Fig. 6A) and forelimb placement task (Fig. 6B) compared to the ICH control group. Additionally, neurological function scores in dECM@exo group rats showed marked improvement within 24 h post-surgery, with sustained enhancement observed over time following dECM@exo administration (Fig. 6C and D).

dECM@exo reduces inflammatory response in ICH rats

Post-ICH, leukocyte counts in the peripheral blood of rats were quantified. Results demonstrated a significant increase in white blood cell counts following ICH, which were effectively suppressed by dECM@exo treatment, particularly at the 24-hour mark post-ICH. dECM alone did not demonstrate the same effect (Fig. 6E). ELISA analysis revealed increased levels of pro-inflammatory markers IL-1β (Fig. 6F) and TNF-α (Fig. 6G), alongside a reduction in the anti-inflammatory factor IL-10 (Fig. 6H) in the serum of ICH-induced rats. Notably, dECM@exo treatment mitigated these changes. Western blot assays confirmed reduced expression of TLR4, NF-κB/P65, and p-P65 proteins following dECM@exo administration (Fig. 6I and J). Additionally, RT-PCR analysis indicated an upregulation of TLR4 mRNA levels post-ICH, with dECM@exo treatment having no effect on TLR4 mRNA expression (Fig. 6K). In conclusion, administration of dECM@exo effectively alleviates inflammation following ICH (Fig. 7).

dECM@exo reduces apoptosis response in ICH rats

TUNEL staining demonstrated a marked increase in apoptotic cell density post- ICH. Orthotopic implantation of dECM@exo significantly attenuated apoptosis, whereas dECM alone failed to exhibit comparable anti-apoptotic effects.

dECM@exo inhibits ICH-induced excessive inflammation via TLR4/NF-κB signaling pathway

Our experiments confirmed that dECM@exo suppresses TLR4 expression and its downstream target proteins NF-κB/P65 and p-P65, both in vitro and in vivo. To explore the mechanism by which dECM@exo inhibits inflammatory responses, astrocytes were transfected with TLR4-specific siRNA or control fragments and subsequently treated with Hemin after a three-hour interval to establish an ICH model. Western blot analysis showed a significant decrease in TLR4, NF-κB/P65, and p-P65 protein levels in the 24-hour dECM@exo group and TLR4 siRNA group compared to the PBS group (Fig. 8A and B). RT-PCR results indicated that dECM@exo administration did not affect TLR4 mRNA expression, which was significantly reduced in the TLR4 siRNA group (Fig. 8C). Additionally, ELISA results demonstrated that both dECM@exo treatment and TLR4 siRNA transfection significantly lowered levels of IL-1β (Fig. 8D) and TNF-α (Fig. 8E) released by astrocytes and increased IL-10 expression (Fig. 8F). Immunofluorescence staining confirmed a notable reduction in TLR4 expression in astrocytes following dECM@exo treatment or TLR4 siRNA transfection after ICH exposure (Fig. 8G and I). Furthermore, immunofluorescence analysis showed that dECM@exo treatment and TLR4 siRNA transfection inhibited the nuclear translocation of p-P65 in cultured astrocytes in response to ICH stimulation (Fig. 8H and J). Collectively, these findings suggest that dECM@exo mitigates ICH-induced inflammation by attenuating the activity of the TLR4/NF-κB signaling pathway (Fig. 9).

Discussion

In this study, we developed a novel light-sensitive injectable three-dimensional (3D) biological scaffold aimed at targeting neuroinflammation for the treatment of intracerebral hemorrhage (ICH). This innovative scaffold integrates the therapeutic benefits of decellularized extracellular matrix (dECM) and human umbilical cord mesenchymal stem cell-derived exosomes (hUC-MSC-exos), demonstrating enhanced efficacy compared to conventional biological scaffolds [46–50]. Previous research indicates that hUCMSC-exos play a crucial role in inhibiting neuroinflammation by reducing TLR4 activity. The 3D scaffold also prolongs the activity of hUCMSC-exos within the ICH environment, allowing them to remain functional for up to 14 days. By housing hUCMSC-exos, the scaffold facilitates the inactivation of inflammasomes and the reduction of inflammatory factor release, ultimately suppressing inflammation and enhancing neuron survival. This collaboration between dECM and hUCMSC-exos improves neuronal resilience during the early stages of ICH, reducing apoptosis and supporting proliferation. Our findings highlight the

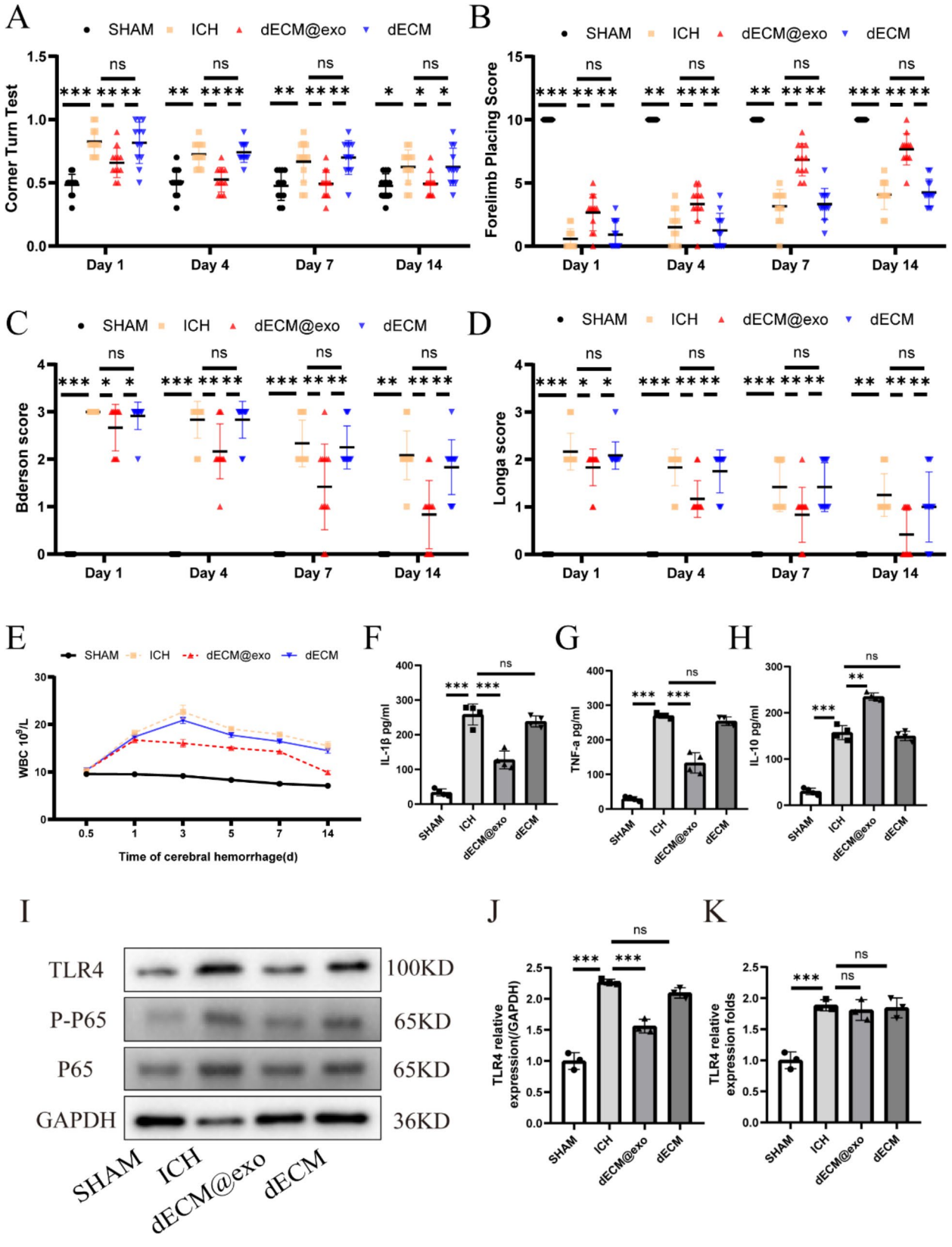

Fig. 6 (See legend on next page.)

(See figure on previous page.)

Fig. 6 dECM@exo reduces the inflammatory response after ICH. (**A**) Corner test ($n=12$). (**B**) Forelimb placement test ($n=12$). (**C**) Bederson and (**D**) Longa scores were performed from day 1 to day 14 after ICH to evaluate the recovery of neurological function ($n=12$). (**E**) Total leukocyte count in different groups ($n=12$). (**F**-**H**) ELISA method was used to detect the concentrations of IL-1β, TNF-α and IL-10 in serum ($n=4$). (**I**) Western blot of TLR4 and NF-κB/P65, p-P65. (**J**) Statistical analysis of TLR4 ($n=3$). (**K**) Statistical analysis of TLR4 mRNA ($n=3$). Data were expressed as mean ± standard deviation. *$p<0.05$, **$p<0.01$, ***$p<0.001$, ****$p<0.0001$

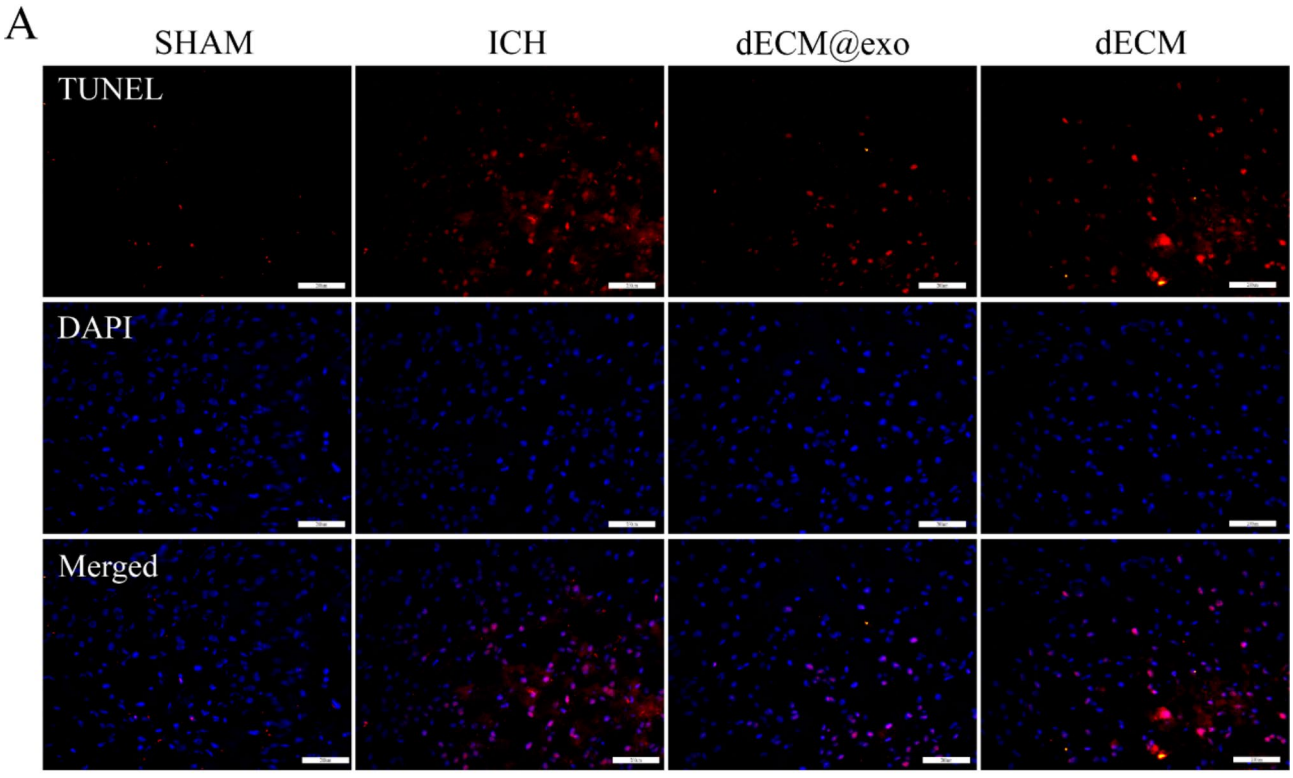

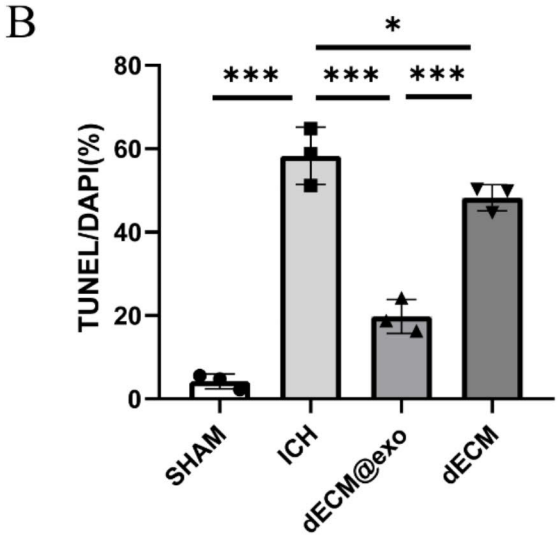

Fig. 7 dECM@exo reduces the apoptosis response after ICH. (**A**) Representative images of TUNEL staining. (**B**) Statistical plot of TUNEL fluorescence ratio ($n=3$). Scale bars: A 200 μm. Data were expressed as mean ± standard deviation. *$p<0.05$, **$p<0.01$, ***$p<0.001$, ****$p<0.0001$

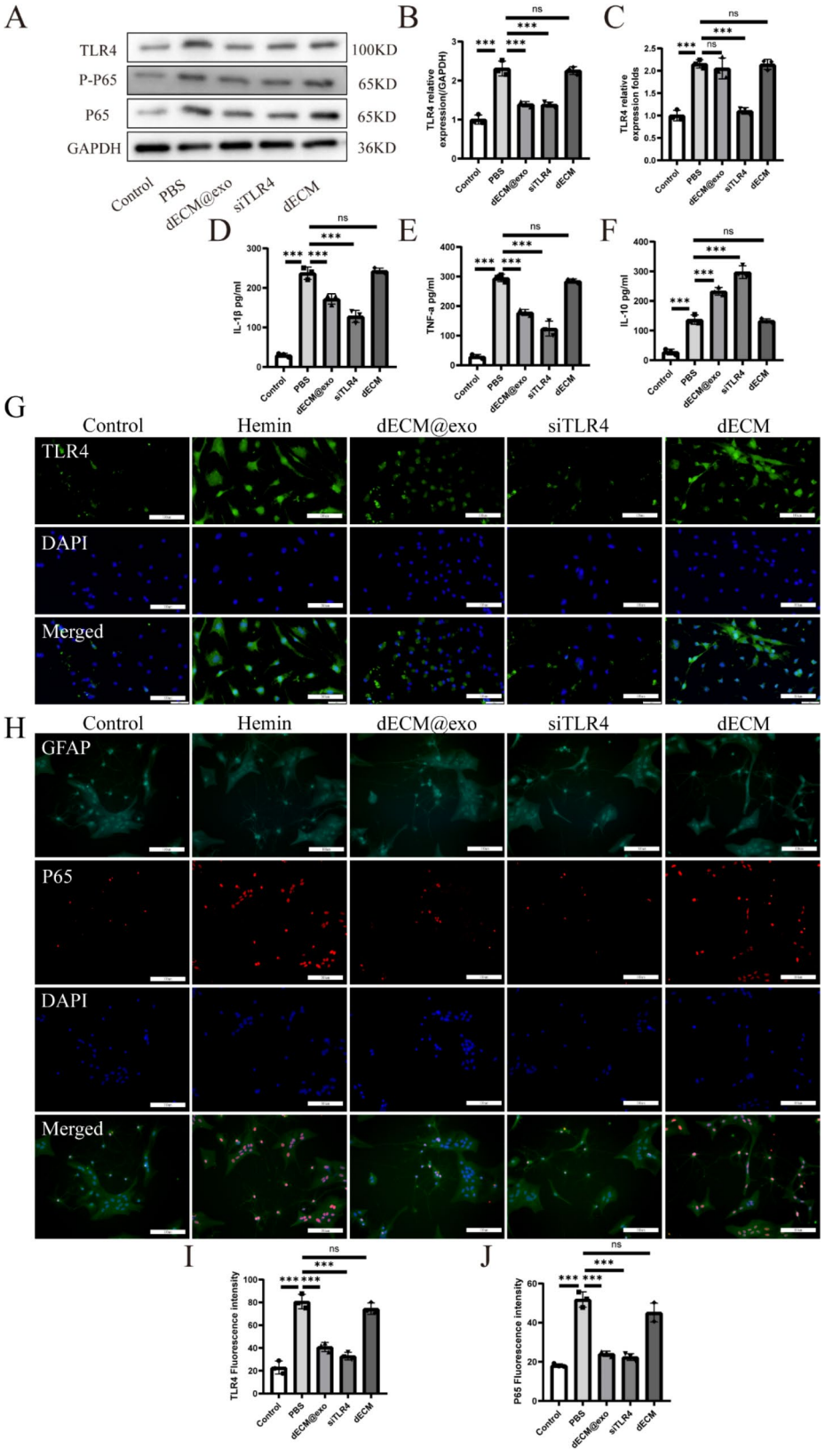

Fig. 8 (See legend on next page.)

(See figure on previous page.)

Fig. 8 dECM@exo inhibits ICH-induced excessive inflammation through the TLR4/NF-κB signaling pathway. (**A**) Western blot of TLR4 and NF-κB/P65, p-P65. (**B**) Statistical analysis of TLR4. (**C**) Statistical analysis of TLR4 mRNA. (**D**-**F**) ELISA analysis of IL-1β, TNF-α and IL-10 levels in different groups ($n = 3$). (**G**) Representative immunofluorescence images and (**I**) statistical analysis of TLR4 expression in astrocytes ($n = 3$). (**H**) Representative images and (**J**) statistical analysis of P-65 nuclear translocation in ICH-induced astrocytes ($n = 3$). Scale bars: G and H 100 μm. Data were expressed as mean ± standard deviation. $^{*}p < 0.05$, $^{**}p < 0.01$, $^{***}p < 0.001$, $^{****}p < 0.0001$

potential of this approach for modulating neuroinflammation and improving ICH treatment outcomes.

The compatibility of dECM@exo with biological systems is robust, as it does not provoke immune responses. Successful decellularization requires a dry weight DNA content below 50 ng/mg, DNA fragments shorter than 200 bp, and the absence of visible nuclear material in DAPI or HE staining [51]. Our results indicate that nearly all cellular components in dECM have been eliminated, mitigating the risk of immune reactions. Recent studies have demonstrated the regenerative capabilities of decellularized rat brain tissue [52, 53], addressing matrix degradation due to metabolic disorders and counteracting the adverse effects of metalloproteinases. Moreover, dECM enhances the extracellular matrix's structural integrity while supporting glial cell proliferation and minimizing inflammatory damage [54]. Importantly, dECM@exo can effectively slow hUCMSC-exos release while maintaining a high loading capacity for hUCMSC-exos.

FTIR spectroscopy confirmed the presence of numerous positively charged groups in the dECM. The zeta potential measurements for hUCMSC-exos indicated a negative charge, demonstrating their ability to bind effectively to dECM through electrostatic interactions, thereby facilitating hUCMSC-exos loading [55]. Other binding mechanisms include integrins on the hUCMSC-exos membrane that interact with the ECM, functioning as cell-like structures through laminin interactions. Comparison of the FTIR spectra of dECM and laminin suggested the presence of laminin in dECM, though additional evidence is necessary to substantiate this claim. Utilizing dECM for hUCMSC-exos loading offers the benefit of a specific delivery mechanism for hUCMSC-exos within the ECM [56, 57]. In vitro studies highlight

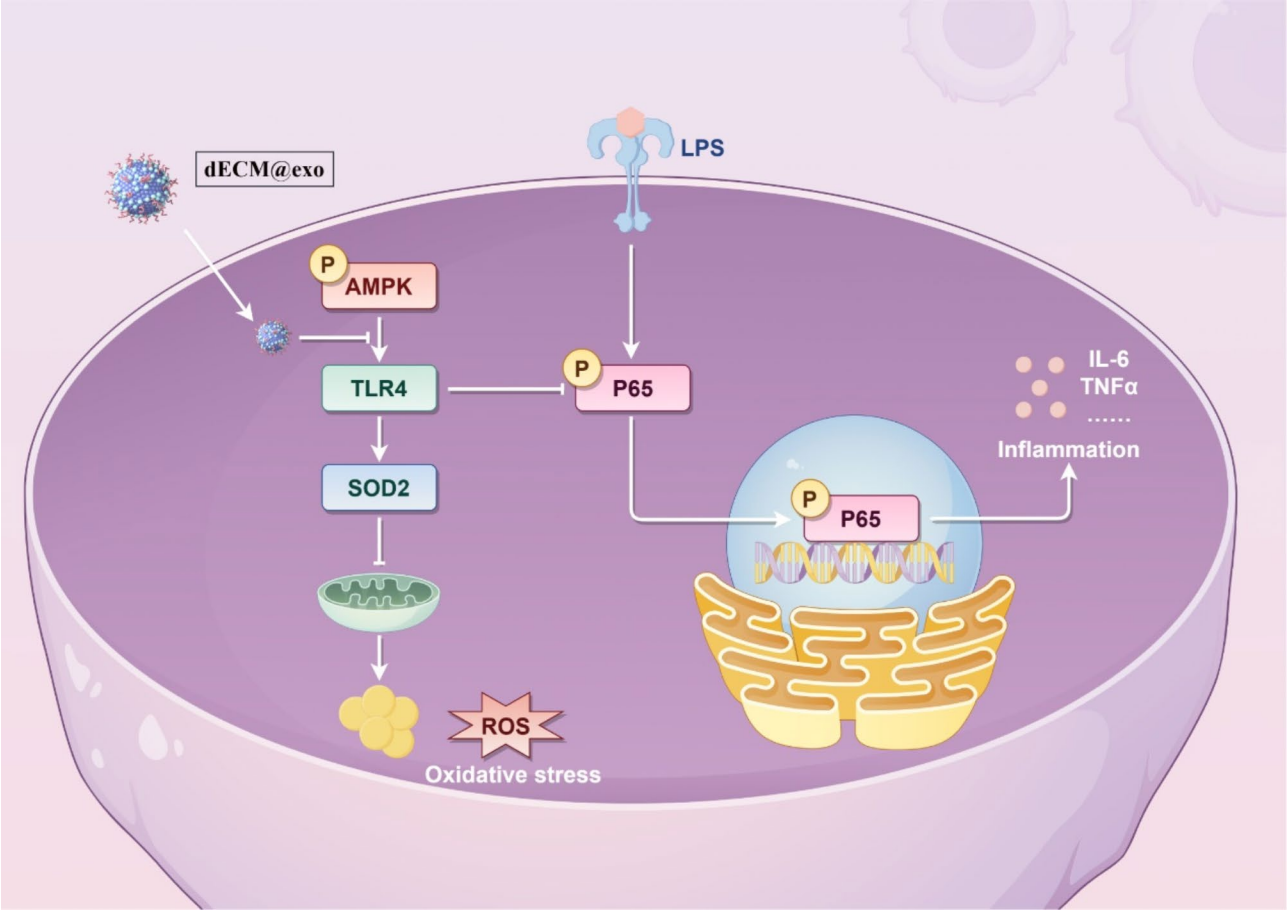

Fig. 9 Effect of dECM@exo on neuroinflammation in rats with cerebral hemorrhage

the advantages of dECM's low modulus for optimal hUCMSC-exos distribution. After injection, the modulus of dECM increases, securing hUCMSC-exos in place, which can then be released within the dECM to target nerve cells due to high cross-linking and surface channel proteins. As nerve cells grow and proliferate within the dECM, they may facilitate intercellular vesicle transport as conduits. This enables targeted drug delivery to nerve cells using dECM@exo loaded with engineered hUCMSC-exos, thereby enhancing the efficacy of small molecule drugs.

The combination of a 3D biological scaffold and exosome therapy presents two novel avenues in ICH treatment. dECM@exo enhances the capacity to promote the proliferation and growth of neural cells, as well as to modulate the metabolism of the extracellular matrix. Although the TLR4/NF-κB pathway was significantly inhibited, exosomes may exert therapeutic effects via alternative signaling pathways, such as PI3K/Akt or Wnt/β-catenin, necessitating further mechanistic exploration through multi-omics analyses (e.g., single-cell RNA sequencing) [58]. Nanoparticle tracking analysis (NTA) revealed that approximately 12% of administered exosomes entered systemic circulation via cerebrospinal fluid (CSF), potentially diminishing targeted efficacy and inducing off-target systemic effects. To address these challenges, future studies will focus on: (1) Microfluidic optimization: Enhancing exosome loading consistency and scalability to minimize batch-to-batch variability. (2) Stimuli-responsive design: Incorporating ROS/pH-sensitive motifs to enable inflammation-triggered exosome release within pathological microenvironments. (3) Miniaturized scaffold fabrication: Reducing scaffold dimensions to $<1\ mm^3$ for compatibility with neuroendoscopic-assisted implantation, thereby minimizing invasiveness and improving clinical feasibility.

Our experimental results demonstrate that this combination effectively suppresses ICH, whereas treatments with dECM or hUCMSC-exos alone yield limited efficacy. Compared to cell therapy, both dECM and hUCMSC-exos exhibit low immunogenicity, which positions dECM@exo favorably for clinical applications. In selecting materials, we prioritized biomaterials with a low rejection likelihood to mitigate cellular rejection and ensure biocompatibility. Additionally, we implemented an efficient method for enriching dECM, reducing the preparation time to just one day, compared to previous methodologies. Our ultimate aim is to advance dECM@exo therapies for clinical use.

Conclusion

In this study, we developed a 3D-printed injectable dECM@exo to modulate the microenvironment following intracerebral hemorrhage (ICH). Our findings confirm the biosafety of dECM@exo and its effectiveness in regulating neuroinflammation, ultimately promoting the recovery of neurological function. Thus, dECM@exo represents a promising new strategy for the development of biotherapeutics aimed at treating ICH.

Abbreviations

ICH	Intracerebral hemorrhage
3D biological scaffold	Three-dimensional (3D) biological scaffold
dECM	Decellularized brain matrix
ECM	Extracellular matrix
hUCMSC-exos	Human umbilical cord-derived mesenchymal stem cell exosomes
MMPs	Matrix metalloproteinases
MSCs	Mesenchymal stem cells
EVs	Extracellular vesicles
MSC-Exo	MSC-derived exosomes
dECM@exo	dECM hydrogels to create hUCMSC-exos -loaded
HE	Hematoxylin and eosin
TEM	Transmission Electron Microscopy
NTA	Nanoparticle tracking analysis
FT-IR	Fourier-transform infrared
SEM	Scanning Electron Microscopy
ELISA	Enzyme-linked immunosorbent assay

Supplementary Information

The online version contains supplementary material available at https://doi.org/10.1186/s13287-025-04332-3.

Supplementary Material 1

Acknowledgements

Not applicable.

Author contributions

Aobo Zhang and Liqiang Liu designed the study and wrote the manuscript. Aobo Zhang, Boyu Sun, Chengrui Nan, Lulu Cong, Zongmao Zhao and Liqiang Liu performed the behavioral testing and experiments and analyzed the data. Aobo Zhang and Liqiang Liu contributed to revising the manuscript. All authors read and approved the final manuscript.

Funding

Central Guiding Local Science and Technology Development Fund Projects (236Z7752G); the Medical Research Project of Hebei Provincial Health Commission (20230031); Special Project for the Construction of Hebei Province International Science and Technology Cooperation Base (193977143D).

Data availability

The data used to support the findings of this study are included in the article.

Declarations

Ethics approval and consent to participate

the original source (Hebei Benyuan Biotechnology) has confirmed that there was initial ethical approval for collection of human cells, and that the donors had signed informed consent. The work has been reported in line with the ARRIVE guidelines 2.0. Title of the approved project: Effects of 3D-Printed Exosome-Functionalized Brain Acellular Matrix Hydrogel on Neuroinflammation in Rats Following Cerebral Hemorrhage. Name of the institutional approval committee or unit: the Second Hospital of Hebei Medical University. Approval number: 2024-R190. Date of approval: 2024.3.4.

Consent for publication

All authors have read the manuscript and provided their consent for the submission.

Competing interests
The authors declare no competing interests.

Author details
[1]Department of Neurosurgery, The Second Hospital of Hebei Medical University, Shijiazhuang 050000, Hebei, China

Received: 28 January 2025 / Accepted: 10 April 2025
Published online: 20 April 2025

References

1. Zhang A, Cong L, Nan C, Zhao Z, Liu L. 3D biological scaffold delivers Bergenin to reduce neuroinflammation in rats with cerebral hemorrhage. J Transl Med. 2024;22(1):946.
2. Nan C, Zhang Y, Zhang A, Shi Y, Yan D, Sun Z, Jin Q, Huo H, Zhuo Y, Zhao Z. Exosomes derived from human umbilical cord mesenchymal stem cells decrease neuroinflammation and facilitate the restoration of nerve function in rats suffering from intracerebral hemorrhage. Mol Cell Biochem. 2025;480(1):309–23.
3. Hao L, Zhang A, Lv D, Cong L, Sun Z, Liu L. EGCG activates Keap1/P62/Nrf2 pathway, inhibits iron deposition and apoptosis in rats with cerebral hemorrhage. Sci Rep. 2024;14(1):31474.
4. Brouwers HB, Goldstein JN. Therapeutic strategies in acute intracerebral hemorrhage. Neurotherapeutics. 2012;9(1):87–98.
5. Babu R, Bagley JH, Di C, Friedman AH, Adamson C. Thrombin and Hemin as central factors in the mechanisms of intracerebral hemorrhage-induced secondary brain injury and as potential targets for intervention. Neurosurg Focus. 2012;32(4):E8.
6. Elliott J, Smith M. The acute management of intracerebral hemorrhage: a clinical review. Anesth Analg. 2010;110(5):1419–27.
7. Lee MJ, Cha J, Choi HA, Woo SY, Kim S, Wang SJ, et al. Blood-brain barrier breakdown in reversible cerebral vasoconstriction syndrome: implications for pathophysiology and diagnosis. Ann Neurol. 2017;81(3):454–66.
8. Lan X, Han X, Liu X, Wang J. Inflammatory responses after intracerebral hemorrhage: from cellular function to therapeutic targets. J Cereb Blood Flow Metab. 2019;39(1):184–6.
9. Selim M, Norton C. Perihematomal edema: implications for intracerebral hemorrhage research and therapeutic advances. J Neurosci Res. 2020;98(1):212–8.
10. Maldonado-Lasunción I, Haggerty AE, Okuda A, Mihara T, de la Oliva N, Verhaagen J, Oudega M. The effect of inflammatory priming on the therapeutic potential of mesenchymal stromal cells for spinal cord repair. Cells. 2021;10:1316.
11. Sakai D, Andersson GB. Stem cell therapy for intervertebral disc regeneration: Obstacles and solutions. Nat Rev Rheumatol. 2015;11:243–56.
12. Kang S, Park JB, Lee TJ, Ryu S, Bhang SH, La WG, Noh MK, Hong BH, Kim BS. Covalent conjugation of mechanically stiff graphene oxide flakes to three-dimensional collagen scaffolds for osteogenic differentiation of human mesenchymal stem cells. Carbon. 2015;83:162–72.
13. Tanwar G, Mazumder AG, Bhardwaj V, Kumari S, Bharti R, Yamini, et al. Target identification, screening and in vivo evaluation of pyrrolone-fused benzosuberene compounds against human epilepsy using zebrafish model of pentylenetetrazol-induced seizures. Sci Rep. 2019;9(1):7904.
14. Mäger SELA, Breakefield I, Wood XO. Extracellular vesicles: biology and emerging therapeutic opportunities. Nat Rev Drug Discov. 2013;12(5):347–57.
15. Phinney DG, Pittenger MF. Concise review: MSC-Derived exosomes for Cell-Free therapy. Stem Cells. 2017;35(4):851–8.
16. Zhang X, Cai Z, Wu M, Huangfu X, Li J, Liu X. Adipose stem cell-derived exosomes recover impaired matrix metabolism of torn human rotator cuff tendons by maintaining tissue homeostasis. Am J Sports Med. 2021;49:899–908.
17. Shi Y, Wang Y, Li Q, Liu K, Hou J, Shao C, Wang Y. Immunoregulatory mechanisms of mesenchymal stem and stromal cells in inflammatory diseases. Nat Rev Nephrol. 2018;14:493–507.
18. Long Q, Upadhya D, Hattiangady B, Kim DK, An SY, Shuai B, et al. Intranasal MSC-derived A1-exosomes ease inflammation, and prevent abnormal neurogenesis and memory dysfunction after status epilepticus. Proc Natl Acad Sci U S A. 2017;114(17):E3536–45.
19. Bhardwaj V, Purohit R. Computational investigation on effect of mutations in PCNA resulting in structural perturbations and Inhibition of mismatch repair pathway. J Biomol Struct Dyn. 2020;38(7):1963–74.
20. Drommelschmidt K, Serdar M, Bendix I, Herz J, Bertling F, Prager S, et al. Mesenchymal stem cell-derived extracellular vesicles ameliorate inflammation-induced preterm brain injury. Brain Behav Immun. 2017;60:220–32.
21. Yang Y, Ye Y, Su X, He J, Bai W, He X. MSCs-Derived exosomes and neuroinflammation, neurogenesis and therapy of traumatic brain injury. Front Cell Neurosci. 2017;11:55.
22. Xian P, Hei Y, Wang R, Wang T, Yang J, Li J, et al. Mesenchymal stem cell-derived exosomes as a nanotherapeutic agent for amelioration of inflammation-induced astrocyte alterations in mice. Theranostics. 2019;9(20):5956–75.
23. Xiang H, Su W, Wu X, Chen W, Cong W, Yang S, Liu C, Qiu C, Yang SY, Wang Y, Zhang G, Guo Z, Xing D, Chen B. Exosomes derived from human urine-derived stem cells inhibit intervertebral disc degeneration by ameliorating endoplasmic reticulum stress. Oxid Med Cell Longev. 2020; 2020:6697577.
24. Hu ZL, Li HY, Chang X, Li YY, Liu CH, Gao XX, Zhai Y, Chen YX, Li CQ. Exosomes derived from stem cells as an emerging therapeutic strategy for intervertebral disc degeneration. World J Stem Cells. 2020;12:803–13.
25. Li Q, Yu H, Sun M, Yang P, Hu X, Ao Y, Cheng J. The tissue origin effect of extracellular vesicles on cartilage and bone regeneration. Acta Biomater. 2021;125:253–66.
26. Mercuri JJ, Patnaik S, Dion G, Gill SS, Liao J, Simionescu DT. Regenerative potential of decellularized Porcine nucleus pulposus hydrogel scaffolds: stem cell differentiation, matrix remodeling, and biocompatibility studies. Tissue Eng Part A. 2013;19:952–66.
27. Chan LK, Leung VY, Tam V, Lu WW, Sze KY, Cheung KM. Decellularized bovine intervertebral disc as a natural scaffold for xenogenic cell studies. Acta Biomater. 2013;9:5262–72.
28. Fiordalisi M, Silva AJ, Barbosa M, Gonçalves R, Caldeira J. Decellularized scaffolds for intervertebral disc regeneration. Trends Biotechnol. 2020;38:947–51.
29. Lu G, Tang R, Nie J, Zhu X. Photocuring 3D printing of hydrogels: techniques, materials, and applications in tissue engineering and flexible devices. Macromol Rapid Commun. 2024;45(7):e2300661.
30. Wang L, Chen P, Pan Y, Wang Z, Xu J, Wu X, Yang Q, Long M, Liu S, Huang W, Ou C, Wu Y. Injectable photocurable Janus hydrogel delivering HiPSC cardiomyocyte-derived exosome for post-heart surgery adhesion reduction. Sci Adv. 2023;9(31):eadh1753.
31. Später T, Mariyanats AO, Syachina MA, Mironov AV, Savelyev AG, Sochilina AV, Menger MD, Vishnyakova PA, Kananykhina EY, Fatkhudinov TK, Sukhikh GT, Spitkovsky DD, Katsen-Globa A, Laschke MW, Popov VK. In vitro and in vivo analysis of adhesive, Anti-Inflammatory, and proangiogenic properties of novel 3D printed hyaluronic acid glycidyl methacrylate hydrogel scaffolds for tissue engineering. ACS Biomater Sci Eng. 2020;6(10):5744–57.
32. Kumar JP, Mandal BB. Antioxidant potential of mulberry and Non-mulberry silk sericin and its implications in biomedicine. Free Radic Biol Med. 2017;108:803–18.
33. Lamboni L, Gauthier M, Yang G, Wang Q. Silk sericin: A versatile material for tissue engineering and drug delivery. Biotechnol Adv. 2015;33:1855–67.
34. Elahi M, Ali S, Tahir HM, Mushtaq R, Bhatti MF. Sericin and fibroin Nanoparticles—Natural product for Cancer therapy: A comprehensive review. Int J Polym Mater. 2020;70:256–69.
35. Sunaina S, Subhayan D, Mahitosh M, Ghosh AK, Kundu SC. Prospects of nonmulberry silk protein Sericin-based nanofibrous matrices for wound Healing—In vitro and in vivo investigations. Acta Biomater. 2018;78:137–50.
36. Zimmermann DR, Dours-Zimmermann MT. Extracellular matrix of the central nervous system: from neglect to challenge. Histochem Cell Biol. 2008;130:635–53.
37. Jakeman LB, Williams KE, Brautigam B. In the presence of danger: the extracellular matrix defensive response to central nervous system injury. Neural Regeneration Res. 2014;9:377–84.
38. Wang S, Wang H, Lu P, Gong L, Gu X, Li M. Mechanisms underlying the cell-matrixed nerve grafts repairing peripheral nerve defects. Bioact Mater. 2023;31:563–77.
39. Castillo GM, et al. Perlecan binds to the β-amyloid proteins (aβ) of Alzheimer's disease, accelerates Aβ fibril formation, and maintains Aβ fibril stability. J Neurochem. 1997;69:2452–65.
40. Busch SA, Silver J. The role of extracellular matrix in CNS regeneration. Curr Opin Neurobiol. 2007;17:120–7.
41. Seon Y, et al. Applications of decellularized extracellular matrix in bone and cartilage tissue engineering. Bioeng Translational Med. 2019;4:83–95. https://doi.org/10.1002/btm2.10110.
42. Garreta E, et al. Tissue engineering by decellularization and 3D Bioprinting. Mater Today. 2017;20:166–78.

43. Beachley V, et al. Extracellular matrix particle–glycosaminoglycan composite hydrogels for regenerative medicine applications. J Biomedical Mater Res–Part A. 2018;106:147–59.
44. Zhang Y, Pizzute T, Pei M. Anti-inflammatory strategies in cartilage repair. Tissue Engineering: Part B. 2014;20:655–68.
45. Han Y, Dong Y, Jia B, Shi X, Zhao H, Li S, Wang H, Sun B, Yin L, Dai K. High-precision bioactive scaffold with dECM and extracellular vesicles targeting 4E-BP Inhibition for cartilage injury repair. Mater Today Bio. 2024;27:101114.
46. Ligorio C, O'Brien M, Hodson NW, Mironov A, Iliut M, Miller AF, Vijayaraghavan A, Hoyland JA, Saiani A. TGF-β3-loaded graphene oxide - self-assembling peptide hybrid hydrogels as functional 3D scaffolds for the regeneration of the nucleus pulposus. Acta Biomater. 2021;127:116–30.
47. Natarajan A, Sivadas VP, Nair PD. 3D-printed biphasic scaffolds for the simultaneous regeneration of osteochondral tissues. Biomed Mater. 2021.
48. Razavi M, Hu S, Thakor AS. A collagen based cryogel bioscaffold coated with nanostructured polydopamine as a platform for mesenchymal stem cell therapy. J Biomed Mater Res A. 2018;106:2213–28.
49. Duan H, Liu Y, Gao Z, Huang W. Recent advances in drug delivery systems for targeting cancer stem cells. Acta Pharm Sin B. 2021;11:55–70.
50. Wu D, Chang X, Tian J, Kang L, Wu Y, Liu J, Wu X, Huang Y, Gao B, Wang H, Qiu G, Wu Z. Bone mesenchymal stem cells stimulation by magnetic nanoparticles and a static magnetic field: release of Exosomal miR-1260a improves osteogenesis and angiogenesis. J Nanobiotechnol. 2021;19:209.
51. Crapo PM, Gilbert TW, Badylak SF. An overview of tissue and whole organ decellularization processes. Biomaterials. 2011;32:3233–43.
52. Wachs RA, Hoogenboezem EN, Huda HI, Xin S, Porvasnik SL, Schmidt CE. Creation of an injectable in situ gelling native extracellular matrix for nucleus pulposus tissue engineering. Spine J. 2017;17:435–44.
53. de Vries S, Doeselaar MV, Meij B, Tryfonidou M, Ito K. Notochordal cell matrix as a therapeutic agent for intervertebral disc regeneration. Tissue Eng Part A. 2019;25:830–41.
54. Mwale F, Roughley P, Antoniou J. Distinction between the extracellular matrix of the nucleus pulposus and hyaline cartilage: a requisite for tissue engineering of intervertebral disc. Eur Cell Mater. 2004;8:58–63. discussion 63–54.
55. Wang C, Wang M, Xu T, Zhang X, Lin C, Gao W, Xu H, Lei B, Mao C. Engineering bioactive self-healing antibacterial exosomes hydrogel for promoting chronic diabetic wound healing and complete skin regeneration. Theranostics. 2019;9:65–76.
56. Chang AC, Uto K, Homma K, Nakanishi J. Viscoelastically tunable substrates elucidate the interface-relaxation-dependent adhesion and assembly behaviors of epithelial cells. Biomaterials. 2021;274:120861.
57. Sun Z, Yang J, Li H, Wang C, Fletcher C, Li J, Zhan Y, Du L, Wang F, Jiang Y. Progress in the research of nanomaterial-based exosome bioanalysis and exosome-based nanomaterials tumor therapy. Biomaterials. 2021;274:120873.
58. Lenzini S, Bargi R, Chung G, Shin JW. Matrix mechanics and water permeation regulate extracellular vesicle transport. Nat Nanotechnol. 2020;15:217–23.

Publisher's note